Real-time evolution of texture and temperature during friction stir processing of a magnesium alloy: an operando neutron diffraction study

Yuan Li[1], Peijun Hou[1], Rakesh R. Kamath[1], Zhili Feng[2], Ke An[3], and Hahn Choo[1,*]

1. Materials Science & Engineering, University of Tennessee, Knoxville, TN 37996, USA
2. Materials Science & Technology, Oak Ridge National Laboratory, Oak Ridge, TN 37831, USA
3. Neutron Scattering Sciences, Oak Ridge National Laboratory, Oak Ridge, TN 37831, USA

*** Corresponding Author:**

Hahn Choo, Ph.D.
Department of Materials Science and Engineering
The University of Tennessee
411 Ferris Hall
Knoxville, TN 37996-2100
Tel 865 974 3643
Fax 865 974 4115
Email: hchoo@utk.edu

*Author to whom all correspondence should be addressed. Electronic mail: hchoo@utk.edu

Abstract

The real-time development of texture and the evolution of temperature during a friction stir processing (FSP) of a Mg alloy were investigated using an operando neutron diffraction measurement technique. A novel neutron diffraction approach was applied in this study where the real-time, quasi-steady state measurements performed as a function of position during FSP are converted to a Lagrangian dataset that reveals the transient behavior as a function of time. The in situ FSP was carried out under two different thermo-mechanical processing conditions represented by the Zener-Hollomon parameter, Z. The results show that: (i) a shear texture develops from the initial strong basal texture with the peak temperature reaching about 775 K during a low-Z processing and (ii) a strong off-normal texture develops with a peak temperature of 640 K during a high-Z processing. Moreover, time-temperature-texture diagrams were established to reveal the transient development of the texture during the real-time processing for both the low Z and high Z processing conditions. The in-situ texture development will be discussed in the context of plausible deformation mechanisms during the FSP: first, as the tool shoulder approaches, as the tool pin approaches, immediately after the stirring, the transient behavior at the wake of the tool pin and then the shoulder, and finally, during cooling.

Keywords: texture, temperature, friction stir welding, magnesium, neutron diffraction

1. Introduction

Solid state joining technique such as friction stir welding (FSW) has become more prevalent in electrical vehicles and aerospace industry because it overcomes the drawbacks of solidification defects and grain growth in fusion welding [1, 2]. Friction stir processing (FSP), a variation of FSW, is a solid state processing technique, which has been applied to control the microstructure by producing a ultra-fine grain structure [3], forming homogenously distributed nanocomposites [4], and tailoring the crystallographic texture [5].

Mg alloys, with the hexagonal-closed-packed (HCP) crystal structure, there is an intrinsic deficiency of slip systems at ambient temperature resulting in a significant plastic anisotropy, poor formability, and tension-compression asymmetry [6, 7]. In Mg alloys, the plastic deformation modes include basal slip, twinning, prismatic slip, and pyramidal slip. The activation of these deformation systems is a function of critical resolved shear stress (CRSS) of each mode, Schmid factor, and grain size [8-10]. The critical resolved shear stresses (CRSS) of these modes at room temperature, e.g., with a ratio of 1:2:4:8 [11], can be insensitive to the manufacturing processes.

On the other hand, the Schmid factor is a function of the grain orientation that can be quite readily manipulated. Therefore, controlling the crystallographic texture of Mg alloys has been an effective way to control the mechanical properties [5, 9, 12]. For example, the poor formability of wrought Mg alloy sheet products is partly due to the strong basal texture (with the basal plane normal predominantly aligned along the normal direction of the plate) and resulting in a plastic anisotropy.

Weakening the initial basal texture by alloying rare-earth elements [13] or Ca could be one way to achieve improved formability . A deep drawing study of a ZE10 alloy (Mg-1Zn-RE) with weakened basal texture were drawn more readily at lower temperatures compared to AZ31 (Mg-3Al-1Zn) with strong basal texture [14]. In the room-temperature Erichsen test with the punch speed of 6 mm/min and blank-holder force of 10 kN, AZMX1110 alloy (Mg-1.3Al-0.8Zn-0.7Mn-0.5Ca) with weakened basal texture exhibited a relatively larger index Erichsen (IE) value of 7.8 mm compared to an IE value of 2.7 mm for an as-rolled AZ31 Mg alloy with a strong basal texture [15].

Alternatively, using various thermo-mechanical processing techniques, the strong basal texture of the hot-rolled Mg alloy plates can also be modified. For example, the changes in the texture of AZ31 Mg alloy plate subjected to a series of hot compression along the normal direction (ND) were investigated as a function of thermo-mechanical input, indexed using the Zener-Hollomon parameter (Z), which is, in turn, a function of temperature and strain rate [10, 16]. The Z parameter exerts a strong influence on the changes in texture, altering the initial strong basal texture to a shear texture, a strong off-ND, and to a combination of off-ND and extension twin textures with the increase in Z. Such changes in texture also resulted in dramatic changes in the subsequent mechanical behavior both in terms of activation of different slip systems and resulting yielding behavior [16]. Xin et. al applied two different processing parameters: 800 rpm, 90 mm/s (Z: 3×10^{14} s^{-1}) and 1600 rpm, 10 mm/s (Z: 1×10^{15} s^{-1}) to FSP AZ31 hot-rolled plates and studied the texture of FSPed Mg plate [17]. They found that shear texture and off-normal texture was formed in the stir zone of the low Z and high Z processed plate, respectively. Kim et. al employed three-dimension finite element analysis (FEA) and polycrystal modeling to simulate the texture around the keyhole of FSPed Mg plate [18]. However, it failed to provide the texture evolution as a function of time.

Moreover, the effectiveness of FSP on modifying the texture and resulting tensile ductility of a hot-rolled Mg alloy plate has also been examined in terms of the Z parameter [5]. After a low-Z FSP (using a high tool rotation speed and a slow travel speed), the initial strong basal texture has transformed into a shear texture. After a high-Z FSP (using a low rotation speed and a high travel speed), the initial basal texture was evolved into a strongly polarized off-ND texture with the basal poles tilted about 40º towards the processing direction. The subsequent tensile ductility (along the processing direction) was increased from about 15% for the as-rolled plate to about 25% for specimens with the shear texture and to about 40% for the off-ND texture samples [5].

The experimental investigations of the material flow [19, 20], grain size refinement [21-23], texture modification [5, 24, 25], residual stress [24, 26, 27], and mechanical properties [5, 23, 28-31] of various alloys subjected to the FSW/FSP have been conducted by post-mortem examinations. The final texture in the stir zone of FSP AZ31 Mg alloy [5, 17, 21, 26, 32-37] can be generally categorized as: (i) shear texture (<0001> // processing direction, PD) for a low Z processing and (ii) off-ND texture (<0001> lies between ND and PD) for a high Z processing. During the FSP, there are five key stages: (i) when the material is subjected to the influence of the tool shoulder, (ii) when the tool pin approaches while under the tool shoulder, (iii) when the pin stirs the material, (iv) when the pin travels away but still under the shoulder at the wake, and (v) when cooling away from the influence of the tool. At these different stages, the thermo-mechanical conditions would vary potentially resulting in a dynamic evolution of the texture. Currently, however, the real-time development of the texture during the FSP of Mg alloys is not clearly understood beyond the apparent correlation between the processing condition and the final texture based on post-mortem evaluations as mentioned above.

For the basic understanding of the transient behavior during FSW/FSP, such as the material flow and temperature evolution, and its role in the development of microstructure and texture; studies involving computational fluid dynamics (CFD) modeling and finite element analysis (FEA) are essential [38, 39]. For example, Yu et. al developed a three-dimensional CFD model to study the material flow and heat transfer during a FSP of AZ31 Mg alloy [40]. Nonetheless, there are numerous challenges in simulating the material and heat flow around the rotating and traveling tool during FSP and the simulation results require rigorous validation using experimental data. To investigate the transient nature of the materials behavior during FSP and for the validation of the simulation results, it is critical to experimentally investigate the development of the texture and temperature during the processing. Therefore, a real-time measurement of the texture and temperature development during FSP has technical and scientific merits. Previously, neutron diffraction has been successfully used for in operando measurements of (i) the lattice strain evolution in a running internal combustion engine [41] and (ii) the temperature evolution during FSP of an Al alloy [42].

In this study, a series of real-time neutron diffraction measurements were conducted to measure the changes in lattice parameters and peak intensities during the FSP of AZ31B Mg alloy plate. First, in-situ quasi-steady state measurements were conducted during the FSP as a function of the distance between the FSP tool pin and the measurement position. Subsequently, the in-situ dataset was converted to a Lagrangian dataset representing a time-revolved, real-time processing data. As a result, the development of the texture will be presented as a function of processing time. Also, based on the measured lattice parameters and the coefficients of thermal expansion, the changes in the temperature during FSP were estimated. Moreover, time-temperature-texture diagrams will be presented to illustrate the transition of the texture from the as-received condition, to the initial approach of the FSP tool, then immediately after the tool pin creating the stir zone, and at the wake of the tool during the cooling. Finally, the transient developments of the texture and temperature as a function of the processing time will be discussed in the context of plausible deformation mechanisms during the FSP under the two different thermo-mechanical inputs, namely the low-Z (higher rpm, slower travel, higher strain rate, and higher peak temperature) and the high-Z (lower rpm, faster travel, lower strain rate, and lower peak temperature) conditions.

2. Experimental details

2.1 Materials, portable FSP machine, and processing conditions

A commercial hot-rolled AZ31B Mg alloy plate was used in this study. The as-received microstructure and texture are presented in Figure 1. The average grain size is about 16 μm and the (0002) pole figure (PF) measured using neutron diffraction shows a strong basal texture. More details on the properties of the as-received Mg alloy can be found in [16]. The as-received Mg alloy plates are about 750-mm long, 178-mm wide, and 6.35-mm thick. A commercial 6061-T6 aluminum alloy plate, with the same dimensions, was used as the backing plate during the FSP.

A portable FSP machine, developed for in situ neutron diffraction measurements [42, 43], was used in this study. The two unique design features are the followings: (i) the neutron beam can access the Mg plate close to the tool pin and diffract to two orthogonal neutron detectors and (ii) tool rotates at a fixed position and the workpiece (i.e., Mg plate) travels during the processing allowing a time-averaged diffraction measurement during a quasi-steady state measurement based on Eulerian coordinates. More details about the quasi-steady state measurement scheme used in this study will be presented in the following section. The FSP tool shoulder and the threaded pin has a diameter of 25 mm and 6.35 mm, respectively. The height of the pin is 5.6 mm. The processing direction (PD) is along the rolling direction (RD) of the plate. The forging force of 8000 N along the normal direction (ND) of the plate was applied by the tool shoulder. Two different processing conditions were used for this study: (i) 1200 rpm tool rotation speed and 0.1 mm/s plate travel speed and (ii) 300 rpm and 1 mm/s. These two conditions correspond to the Zener-Hollomon parameter, Z, of 3.3×10^{12} s^{-1} and 1.2×10^{15} s^{-1} and will be referred to as the low Z (LZ) and high Z (HZ) conditions, respectively, Table 1. The details of the empirical calculations of Z values based on the key FSP parameters used for the Mg alloy can be found in [5, 22, 44-49].

2.2 In situ neutron diffraction measurements during FSP

Neutron diffraction, with its good penetration capability, allows volumetric measurements within the Mg alloy plate (through the Al-alloy backing plates used in this study). The time-of-flight neutron diffraction measurement at the Spallation Neutron Source (SNS) at the Oak Ridge National Laboratory also allows probing multiple reflections from two different sample orientations simultaneously. Moreover, the sample stage at the VULCAN engineering beamline at SNS allows operation of a large manufacturing equipment like the portable FSP machine during an in-situ diffraction. Hence, a neutron diffraction measurement at a dedicated engineering beamline is very well suited for the current study. However, the time-of-flight (TOF) neutron diffraction at a spallation source provides a relatively low flux for a time-resolved measurement of a dynamic changes in the microstructure during the FSP. Specifically, the temporal resolution required to probe a transient behavior as the FSP tool approaches and passes by an observation point is too demanding for the TOF neutron diffraction. Therefore, we employed a unique approach of: (i) conducting a series of quasi-steady state measurements that allow us to acquire time-averaged diffraction patterns as a function of the distance between the FSP tool and measurement position and (ii) converting such dataset into a time-resolved snapshots during the FSP to examine the transient behavior. A detailed neutron diffraction measurement procedure used in this study is provided below.

Figure 2 shows a top view of the experimental setup used for the in-situ neutron diffraction measurements carried out at the VULCAN engineering beamline. The portable FSP machine was placed sideways on the sample stage with the scattering geometry set up to allow simultaneous diffraction measurements from two different orientations. As mentioned earlier, the FSP tool rotates at a fixed location and the Mg plate travels along the RD direction of the plate (yellow arrow). Note that the processed region behind the FSP tool is marked by a green box. The scattering volume (marked by a red box) is 2 × 3 × 2 mm^3, defined by a radial collimator (2 mm wide) and an incident beam slit (3 mm × 2 mm). The diffraction data with the scattering vector parallel to RD (//PD) are recorded on the detector bank1 and the data with the scattering vector parallel to ND on the detector bank 2. Using this setup, a series of in-situ quasi-steady state measurements were conducted as a function of the distance between the scattering volume (i.e., the measurement location) and the tool pin, for each distance case using a new Mg plate. A series of other measurement locations are also marked with red boxes (dotted line) in Figure 2.

Once a measurement location in the plate is determined, the scattering volume is defined. Figure 2 shows an example where the measurement location (marked by a red box) is a few millimeters behind the tool pin in the processed zone. Once the stationary FSP tool starts to rotate (e.g., at 1200 rpm), the diffraction measurement starts at that fixed location, while the Mg plate travels as indicated by the arrow providing fresh material at a given travel speed (e.g., at 0.1 mm/s). During this in-situ measurement, the measured diffraction peak position and intensity reach a steady state and it is assumed that the states of the material such as temperature and material flow are in a quasi-steady state [42, 43]. Therefore, from each measurement location, a time-averaged diffraction pattern with good statistics was collected during such quasi-steady state as long as the Mg plate was fed to the scattering volume. The measurement duration was about 30 ~ 60 minutes for each LZ case and about 10 minutes for each HZ case, varying slightly depending on the measurement location. Next step is to repeat the same process with a scattering volume defined at a different distance away from the tool pin using a new Mg plate. The procedure is repeated until all desired positions are probed under the given FSP condition.

Figure 3 presents the specific details of the time-averaged diffraction measurements conducted as a function of distance between the tool pin and the measurement position (Figures 3a,b) as well as their conversion to a time-revolved dataset representing a real-time evolution of diffraction data during the processing (Figure 3c). First, Figure 3a shows all measurement locations including: the scattering volume in front of the pin (unprocessed zone) at -9 mm, and -6 mm; and behind the pin (processed zone) at 6 mm, 7.5 mm, 9 mm, 10.5 mm, 12 mm, 15 mm, and 18 mm. These positions are also visualized with red boxes in Figure 3b. Note that the measurement at -15 mm (blue box) represents a reference measurement where diffraction measurement was conducted before the FSP process was started. The distance is from the center of the FSP tool pin to the center of the scattering volume. All the measurement positions are along the FSP centerline and at the middle of the plate thickness. Note that the RD diffraction data (on bank1) were blocked by the FSP tool shoulder at measurement positions of -9 mm and -6 mm and, hence, not available. These quasi-steady state, time-averaged diffraction data measured from different locations are analyzed to obtain lattice spacings and integrated peak intensities for all available hkls from the two detector banks and the results will be presented in Section 3 for the RD (//PD) and ND orientations and for the LZ and HZ cases.

This dataset, however, is different from the data obtained from a more conventional Lagrangian measurement scheme where the FSP tool travels across the plate. Therefore, the diffraction data measured at different positions is, subsequently, converted to a dataset representing time-resolved snapshots of the transient state of the material at different timeframe during the FSP as shown in Figure 3c. In summary, the quasi-steady state diffraction data measured as a function of the distance between the tool pin and the measurement location (based on Eulerian coordinates) are converted to a set of Lagrangian data representing the temporal evolutions of lattice parameters and intensities as a function of the FSP time. In Figure 3c, the time of 0 s (position of -15 mm) indicates that the FSP has not started yet. Then, the elapsed time during the processing was calculated using the travel speed of the plate and -15 mm as the starting reference point. In the LZ case shown here, the elapsed time corresponding to the distance of -9 mm is 60 s (i.e., 6 mm of travel at 0.1 mm/s speed). In the following section, the lattice parameter and intensity data obtained from these diffraction measurements will be presented in terms of both distance and time.

2.3 Pole figure measurements of the FSP plates

The post-mortem texture measurements were also conducted at the VULCAN beamline using cylindrical samples (5 mm in diameter and 5.5 mm in height) extracted from the stir zone of the FSP plates processed at LZ and HZ conditions as well as from an as-received plate. Using the neutron beam size of 5 × 5 × 5 mm^3 and the texture sample set up on a goniometer, full pole figure measurements were conducted with the Ψ changing from 0° to 90° with steps of 15° and the φ self-rotating from 0° to 330° with steps of 30°. The measurement time for each step was 80 s. The pole figure data was analyzed using the MTEX, a quantitative texture analysis software [50].

2.4 Measurement of coefficient of thermal expansion of AZ31 Mg alloy

The coefficient of thermal expansion (CTE) of AZ31 Mg alloy was measured by conducting an in-situ heating experiment using high-energy synchrotron x-ray diffraction at the Advanced Photon Source at the Argonne National Laboratory. The as-received Mg alloy with a cross-section of 5 mm × 6 mm was heated with a heating rate of 20 K min to temperatures of 298, 358, 418, 478, 538, and 598 K. At each temperature, the sample was held for 3 mins and the diffraction patterns were measured. The Rietveld refinement was performed to obtain the lattice parameters using GSASII [51]. The measured lattice parameters and the CTE can be expressed as a function of temperature from 298 to 598 K by:

$$\bar{a}(T) = 3.64 \times 10^{-10}T^3 - 3.89 \times 10^{-7}T^2 + 2.35 \times 10^{-4}T + 3.82 \qquad (1)$$

$$\alpha(T) = 2.83 \times 10^{-10}T^2 - 2.01 \times 10^{-7}T + 6.08 \times 10^{-5} \qquad (2)$$

$\bar{a}$ is the average lattice parameter where $\bar{a} = (2a + c)/3$ and α is the average CTE [52]. The measured lattice parameters and CTE agree very well (R^2 over 0.99) with those in the literature for the pure Mg [53] and for AZ31 Mg [54, 55].

3. Results

3.1 Neutron diffraction patterns measured during FSP

Figures 4 presents the schematics of the measurement setup and the series of diffraction patterns measured continuously during the FSP. Figure 4a shows an example of the in-situ diffraction measurements at the position of +10.5 mm from the FSP tool pin in the processed region under the low-Z condition. It presents three snapshots at different timeframes of the diffraction measurements as the tool is rotating and the plate is traveling providing fresh material into the scattering volume that is subjected to the same processing history. Figures 4b shows the corresponding contour plot of time-of-flight neutron diffraction patterns of d-spacing (y-axis) vs. intensity (z-axis with a color scale), evolving as a function of time (x-axis). Figure 4b was constructed using the diffraction data collected with the scattering vector parallel to RD (i.e., RD data). Simultaneously, the diffraction patterns were also collected with the scattering vector parallel to ND (i.e., ND data) and the results are presented in Figure 4c. Note that the d-spacing range shown here is a subset of the full diffraction pattern. The contour plots show the evolutions of d-spacings and intensities of $(10\bar{1}0)$, (0002), and $(10\bar{1}1)$ reflections during about 60 minutes of continuous measurements during the FSP. The Rietveld refinement analysis of these diffraction patterns showed that the lattice parameters (a and c) and the integrated peak intensities (I) indeed reached a steady state during which time-averaged lattice parameters and intensities are obtained. These results will be presented in Figures 5 and 6 in the next section.

3.2 Intensity evolution during FSP

The changes in the integrated peak intensities during the FSP is presented using (0002) and $(10\bar{1}1)$ reflections for both LZ and HZ conditions in Figure 5. Figure 5a shows the (0002) intensity evolution measured during the LZ FSP. First, the intensities of the (0002) pole along ND (black square) is presented as a function of the distance between the tool pin and the measurement position ranging from -15 mm (reference point on the unprocessed side) to +18 mm (on the processed side) using the top x-axis. Note that the y-axis error bar on the data represents the fluctuations in the intensity during the measurement, which indicates that the variations in the intensity during the measurement period is negligible and the quasi-steady state was indeed achieved. This was the case for all measurement cases. The x-axis error bars on the data indicates the spatial averaging across the neutron scattering volume.

Initially, the (0002) intensity along ND is relatively strong as expected from the basal texture of the as-received plate (Figure 1b). But, the (0002) intensity decreases significantly under the tool shoulder and closer to the pin. Behind the pin and in the processed region, the (0002) intensity decreased further and remained quite weak. On the other hand, the (0002) intensity along PD (//RD) was initially almost zero (i.e., initial as-received plate texture). The PD (0002) remained weak but increased slightly further away from the pin in the processed region (beyond about +9 mm). After the LZ processing, the (0002) intensities are relatively weak but present along both ND and PD.

Moreover, also presented in Figure 5a is the intensity evolution as a function of the processing time using the bottom x-axis. Note that this illustrates the situation of “moving tool case” obtained from the measured “moving plate case” as explained in Section 2.2. The time-resolved snapshots of the intensity evolution reveal that the (0002) intensity along ND was initially strong (0 s), rapidly decreased under the tool shoulder (60 s), further decreased closer to the pin (90 s), decreased to a minimum after the stirring (at about 210 s), and then remains relatively weak and constant at the wake of the processing as the tool travels away (about 210 ~ 330 s). Note that the tool pin arrives at the observation point at 150 s in this case and blocks the neutron data from the Mg plate. The (0002) along PD shows that the intensity increases slightly at the wake of the processing with time (about 210 ~ 330 s).

Meanwhile, the $(10\bar{1}1)$ intensities evolve as presented in Figure 5b. The $(10\bar{1}1)$ intensity along ND was initially very weak but increased gradually under the tool shoulder in front of the tool pin and continued to increase behind the pin at the wake. The $(10\bar{1}1)$ intensity along PD was relatively stronger, showed a decreased intensity behind the pin, and then increased back again noticeably at the wake.

For the case of HZ FSP (Figures 5c), the (0002) along ND behaved similarly compared to that of LZ case but the intensity dropped much lower when the tool initially approached (at 6 ~ 9 s) and further decreased to near zero at the wake after the stirring. Note that the process was also ten times faster due to the faster travel speed. The (0002) along PD remained near zero during the entire process unlike the LZ case where a slight increase at the wake was observed. The (0002) poles would be almost completely missing along ND and PD on the reconstructed PF at the end of the HZ processing unlike for the case of LZ where (0002) intensities should be observed along both orientations.

Finally, the $(10\bar{1}1)$ intensity evolution during the HZ processing is shown in Figure 5d. The difference between the LZ and HZ cases are more obvious here. The $(10\bar{1}1)$ along ND never develops unlike the LZ case, whereas the increase in $(10\bar{1}1)$ intensity along PD at the wake is much more significant compared to the LZ case.

Here the changes in the intensities of only two reflections were presented to illustrate the transient behavior, but, later in Section 4, the texture changes during FSP and the effect of Z input will be discussed further using PFs reconstructed using the intensity data of all measured reflections.

3.3 Lattice parameter evolution during FSP

Figure 6 presents the changes in the lattice parameters (both a and c for the Mg) during the LZ and HZ FSP. The lattice parameter data is presented here using the same scheme used for the intensity data in Figure 5. Also, note that the error bars shown for the lattice parameter data are adequate for both spatial and temporal analyses. Figures 6a,b show the lattice parameters measured during the LZ processing. Both a and c parameters from ND and PD orientations exhibit similar trends. The initial reference lattice spacing, measured before the processing (at -15 mm and 0 s), increased rapidly as the tool approached, reached a maximum, and gradually decreased as the tool traveled away. The changes in lattice parameters could be caused mainly by the changes in the elastic lattice strain and the temperature from the localized frictional heating and the stirring from the tool shoulder and the pin [42, 56-58]. These two effects on the changes in lattice parameters will be deconvoluted and the development of temperature during FSP will be assessed in Section 4.

Figures 6c,d show the evolutions of a and c lattice parameters during the HZ processing. The HZ data clearly show that the increases in the lattice parameters are much less significant compared to the LZ case. This observation seems reasonable in that the HZ process is the case with a lower rpm and faster travel speed where the corresponding strain rate and the peak temperature in and around the stir zone would be much lower than the LZ case (Table 1).

4. Discussion

4.1 Reconstruction of (0002) pole figures for the analysis of transient texture development

The in-situ neutron diffraction scheme used in this study allowed probing the evolutions of multiple diffraction peak intensities while processing the Mg alloy using a relatively large manufacturing equipment, which is one of the advantages of the time-of-flight neutron scattering at a dedicated engineering beamline. However, the experimental setup permitted rather limited detector coverages at ± 90° 2θ (Figure 2), which was not adequate for in-situ pole figure (PF) measurements. However, the investigation of in-situ development of texture during FSP would benefit from assessing PFs in addition to the limited observations of the intensity evolutions along ND and RD. For example, Yu et al., based on their post-mortem texture analysis [59], showed that the FSP Mg alloy plate exhibits characteristic distributions of (0002) poles along ND-RD plane depending on the processing conditions. To this end, (0002) PFs are reconstructed to investigate the in-situ development of texture during FSP using the intensity data of all reflections available from the ND and RD (//PD) detectors.

First, it was assumed that (i) there is a preferred variant selection along the FSP direction (i.e., RD//PD) and (ii) each texture component is spread over 15 degrees concentrically. Then, the distribution and magnitude of (0002) pole intensity on the PF were determined using a combination of: (i) directly measured (0002) intensities along ND and RD and also (ii) calculated (0002) intensities based on the intensities of other reflections measured along ND and RD.

4.1.1 Distribution of (0002) poles

Figure 7 shows the reconstruction of the distribution of (0002) poles on the (0002) PF using measured intensities of (0002), $(10\bar{1}5)$, $(10\bar{1}3)$, $(10\bar{1}2)$ and $(10\bar{1}1)$ from the ND and RD(//PD) neutron detectors. Figure 7a shows the angular positions of (0002) poles rendered on the PF according to the $(10\bar{1}l)$ poles measured along ND. For example, from the $(10\bar{1}1)$ intensity measured at the ND neutron detector (black arrow), the (0002) intensity can be rendered at 62° away from ND towards RD on the ND-RD plane (red circle). Similarly, from all $(10\bar{1}l)$ intensities measured on the ND detector (black arrows), the distribution of (0002) poles (red circles) can be obtained. Therefore, the four red circles in Figure 7a mark the (0002) variants selected on the ND-RD plane towards the RD(//PD) orientation based on our assumption stated earlier. Note that the angles between $(10\bar{1}l)$ and (0002) for the Mg alloy are summarized in Table 2. Moreover, Figure 7b shows that the $(10\bar{1}l)$ intensities measured at the RD(//PD) neutron detector provide four additional (0002) pole locations as marked. For example, from $(10\bar{1}1)$ intensity measured at the RD(//PD) neutron detector (black arrow) would allow rendering of the (0002) intensity at 28° away from ND (as marked by the red circle). Figure 7c summarizes the distribution of (0002) poles on the (0002) PF that can be rendered using the data from all $(10\bar{1}l)$ and (0002) itself measured on the ND and RD detectors.

4.1.2 Intensity of (0002) poles

The magnitudes of the (0002) pole intensities at the center, north pole, and south pole are measured directly from the neutron diffraction, but for the other pole locations shown in Figure 7c, it is necessary to calculate the intensities from the measured $(10\bar{1}l)$ intensities. The normalized integrated intensity (I_{hkil}) of a plane ($hkil$) in the time-of-flight neutron diffraction is proportional to [60]:

$$I_{hkil} \propto \left(\frac{\lambda^4 m F_{hkil}{}^2}{\sin^2\theta}\right)\left(\frac{N_c}{V}\right) \quad (3)$$

where λ is the wavelength of neutron, m multiplicity of the reflection, F_{hkil} structure factor of the reflection, θ scattering angle, N_c the number of unit cells contributing to the scattering within the scattering volume, V. During the current time-of-flight neutron diffraction measurement, 2θ is fixed at 90° and the λ is proportional to the time-of-flight and, in turn, the d-spacing of a reflection according to the Bragg's law. The multiplicity of (0002) plane is 2 and that of $(10\bar{1}l)$ planes is 12. N_c is often referred to as a reduced intensity and used to express the texture [26, 28]. However, N_c was considered constant for different reflections along with θ and V. Therefore, the theoretical calculation of the intensity ratios between $(10\bar{1}l)$ and (0002) summarized in Table 2 are based on a random texture case. Subsequently, however, by using the measured intensities of $(10\bar{1}l)$ and the theoretical intensity ratios, the textured intensities of (0002) are rendered. For example, the normalized intensity ratio between (0002) and $(10\bar{1}2)$ is 1 to 0.43. Hence, the calculated intensity of (0002) would be 2.33 times the measured intensity of $(10\bar{1}2)$.

4.1.3 Comparison between reconstructed and measured (0002) PFs

By combining the distribution of (0002) poles and their intensities calculated from the (0002) and $(10\bar{1}l)$ reflections, the (0002) PFs are rendered. Figure 8 presents the comparison between the reconstructed and measured (0002) PFs in the stir zone at the end of the FSP for both LZ and HZ conditions. Note that the reconstructed PFs (Figure 8a) are prepared following the procedures described above and the measured PFs (Figure 8b) are obtained from a post-mortem texture measurement (with a full pole coverage) on extracted cylindrical samples from the FSP plates.

For the LZ case, the reconstructed PF shows the characteristic spread of the intensity between the ND and RD with a significantly weakened initial basal texture along ND and a new maximum near 30° from ND. The intensities at the north and south poles are clearly rendered as well. This is in a good agreement with the measured PF in terms of both the distribution and the intensity. Moreover, our assumption of preferred variant selection on the ND-RD plane along RD direction seems to be reasonable. In the measured PF, however, the spread of poles is a little bit wider and the overall intensity distribution seems to be rotated counter clockwise by about 20° near RD. For the HZ case, there is an excellent agreement showing a single, strong component near 30° off ND.

Generally, two different types of texture have been reported for the stir zone of the FSW/FSP Mg plates in the literature [5, 17, 21, 26, 32-37]: (i) a shear texture where <0001> is near parallel to the PD (which is typically parallel to RD) and (ii) an off-ND single-component texture where <0001> lies between ND and PD. It was shown that the (0002) plane prefers to coincide with the shear surface of the tool pin and tool shoulder during an FSW/FSP under processing conditions close to a low-Z condition [33, 61-64]. This type of shear texture is also found in the Mg alloys manufactured using other techniques. For the equal channel angular processing (ECAP) of Mg alloys [65, 66], it was found that basal plane tilted 45° from the extrusion axis, parallel to the shear plane. Also, the typical basal texture of rolled Mg alloy plates can be understood that (0002) plane tends to align parallel to the shear surface of the rolls. On the other hand, the final texture of the HZ case is a strong off-normal texture. Recently, a constitutive study was conducted on the effect of the Z parameter during a hot compression on the texture and the recrystallized grain size [16]. It was shown that, above Z of about 10^{14} s^{-1}, the dynamic recrystallization is preceded by a significant twinning, which results in much finer recrystallized grains forming within the twinned daughters along with a strong off-ND texture component. Also, the "stop-action" studies on the texture of AZ31 during FSP [37, 64] reported the observation of extension twins in front of the tool pin along with the off-ND texture in the stir zone. Figure 8c shows the optical micrographs of the stir zone of LZ and HZ cases, respectively. The average grain size for the LZ case is 22 (± 10) µm and that for the HZ case is 5 (± 2) µm. Compared to the grain size of the as-received specimen (16 ± 7 µm), the grain size increased for the LZ case, whereas a significant refinement was observed for the HZ case, which is consistent with the constitutive study where the twin-assisted dynamic recrystallization resulted in a significant grain refinement along with a strong off-ND texture [16, 22].

Based on the good agreements with the post-mortem textures shown in Figure 8, the same reconstruction procedure was performed for all in-situ neutron diffraction data to assess the temporal evolution of (0002) PFs during FSP, which will be discussed in Section 4.3. But, first, let us discuss the estimation of the temperature evolution during FSP using the measured lattice parameter data in the next section, so that the time-temperature-texture correlation can be discussed subsequently.

4.2 Assessment of temperature evolution during FSP

From the changes in lattice parameters (*a* or *c*) during FSP (Figure 6), the lattice strains can be obtained using: $\varepsilon^a = (a - a_o)/a_o$, where a is the lattice parameter under the influence of FSP (i.e., due to the stress and temperature) and a_o is the reference (stress-free and ambient-temperature) lattice parameter measured at t = 0 s (or at -15 mm) before the processing. For the Mg alloy, the average lattice strains of $\varepsilon_i = 2/3\varepsilon_i^a + 1/3\varepsilon_i^c$ (where *i* = RD//PD~~, TD,~~ and ND) were obtained [52]. Figures 9a and 9b show the changes in the lattice strains of ε_{RD} and ε_{ND} measured during the processing under the LZ and HZ conditions, respectively. It should be noted that these apparent lattice strains measured in situ using neutron diffraction contain both elastic and thermal strain components.

The temperature profile can be obtained from this thermal strain component following the procedure described by Woo et al. [42, 67]. First, the thermal strain (ε_{th}) during the processing can be expressed by:

$$\varepsilon_{th} = \left[\frac{\nu}{1+\nu}(\varepsilon_{RD} + \varepsilon_{TD}) + \frac{1-\nu}{1+\nu}\varepsilon_{ND} + \frac{2\nu-1}{E}\sigma_{ND}\right] \tag{4}$$

where ε_{RD}, ε_{TD}, and ε_{ND} refers to the apparent lattice strain measured along RD, TD, and ND of the plate; ν is the Poisson's ratio; E is Young's modulus, and σ_{ND} is the stress along ND of the plate. Due to the geometrical difficulty of measuring the diffraction along TD during the in situ FSP, we assume that $\varepsilon_{TD} \approx \varepsilon_{RD}$. According to Woo et al. [43], the measured ε_{TD} and ε_{RD} of the Mg alloy after the FSP was very comparable. A constant Poisson's ratio ν of 0.35 was used because of its weak temperature dependence. The temperature (in K) dependent Young's modulus E (in MPa) was obtained by fitting the data available in the literature [55]:

$$E(T) = 0.19T^2 - 209.27T + 86074 \tag{5}$$

σ_{ND} was assumed negligible outside the FSP tool (based on plane stress condition) but was estimated at about -17 MPa under the tool (based on the ratio of forging force and the tool shoulder area).

The thermal strain (ε_{th}) can also be estimated based on the measured coefficient of thermal expansion, $\alpha(T)$, presented in Equation (2).

$$\varepsilon_{th} = \int_{298}^{T} \alpha(T)dT \tag{6}$$

By combining Equations (2), (4), (5), and (6) and solving it for T, we obtained the temperature profiles, presented in Figures 9c and 9d.

Qualitatively, the temperature profiles of the LZ and HZ cases are quite similar in that the temperature increased rapidly as the tool approached and then dropped sharply as the tool pin traveled away. When the scattering volume is outside the tool shoulder (beyond +12 mm at the wake), the cooling seems to slow down significantly from the linear cooling under the shoulder. Specifically, the most striking difference between the two cases are the peak temperatures, which are 775 K and 640 K for the LZ and HZ conditions, respectively. These peak temperatures are comparable to the values estimated empirically, namely 783 K and 608 K (Table 1). Note that even though the peak temperatures for both cases were observed on the wake side, the temperature differences between either side of the tool pin were small. Also, the heating and cooling rates under the shoulder are rather symmetric for both cases. However, even though the HZ case exhibits a lower peak temperature than the LZ case, the rates of temperature change under the shoulder for the HZ case were about 14 times faster during heating and about 9 times faster during cooling compared to the LZ case. In summary, compared to the LZ case, the HZ processing was overall much shorter processing (33 vs. 330 s), reached a lower peak temperature (640 vs. 775 K), and exhibited faster heating and cooling rates (19 vs. 1.4 K/s for heating and 16 vs. 1.7 K/s for cooling).

4.3 Time-temperature-texture diagram: texture development during FSP

The time-temperature-texture diagram is presented in Figure 10. The developments of the texture during the FSP are shown in terms of the (0002) PFs as a function of the processing time for both LZ and HZ conditions. Also presented in the diagram is the temperature profile. The center of each PF marks the corresponding temperature. Note that the (0002) PF at t = 0 s was also reconstructed for consistency, following the Von Mises–Fisher distribution with a 15° angle range.

During the LZ processing, under the tool shoulder as the tool initially approached (60 s, top x-axis), the strong basal texture weakened at ND and spread towards RD at about 730 K. About 6 mm away from the pin surface (90 s), the temperature reached 772 K and the ND intensity weakened further and the intensity spread a little more. After the pin stirred through and at 6 mm behind the pin in the wake (210 s), the intensity is spread even more widely between ND and RD. The change caused by the stirring of the pin is somewhat subtle when comparing the PFs at 6 mm in front of and behind the pin (90 s vs 210 s). The main difference is the appearance of a new maximum between 30° ~ 50° from ND, while still maintaining some intensity at ND. At 9 mm from the pin at the wake (240 s), still under the shoulder, the temperature dropped to about 720 K and a new component developed along RD (both north and south poles). At this stage, a typical shear-type texture was fully formed. This type of texture is often observed in the FSW Mg alloy plates where the (0002) planes are aligned with the shear surfaces of the tool shoulder and pin. Subsequently, as the tool traveled away and the temperature dropped further down to about 670 K (270 s), the texture characteristics remained similar but the RD component became stronger and the maximum between 30° ~ 60° off ND further intensified.

There are two subtle observations worth exploring. First, the RD component (at north and south poles) is often attributed to the shear component caused by the tool pin surface. However, the RD component did not appear immediately after the stirring at 210 s but first observed at 240 s with some delay and further intensified at 270 s. It is plausible that an optimal combination of strain rate and temperature would be needed at the wake of the tool pin for the RD component to form. Similarly, the shear component formed by the tool shoulder (i.e., smearing of the ND component along ND-RD plane) also did not appear instantaneously but took time to develop starting from 60 s to 210 ~240 s. Alternatively, at the wake of the current LZ FSP, the processing condition would shift towards an HZ condition away from the pin. Although the strain rate would decrease moving away from the tool pin, the rapid decrease in temperature could more than compensate it and gradually increase the Z parameter at the wake. This condition could promote some twinning, potentially contributing to the increasing intensity of the RD component.

Secondly, away from the tool shoulder during cooling at about 630 K (330 s), the RD component weakened somewhat and also the previous maximum shifted closer to 30° and concentrated. At this point, since the materials is out of the tool shoulder, it is mostly subjected to a static annealing. It has been reported that the twin is unstable upon annealing at 623 K and generates a recrystallization microstructure [68-70]. For example, when Song et al. annealed equal channel angular rolled Mg plate with the basal and extension twin texture at 623 K, the extension twin texture disappeared and a 40° off-ND texture was formed and intensified. In the current LZ case, the weakening of RD component and the slight shift of the maximum intensity towards 30° may be attributed to the similar effect.

In comparison, during the HZ processing, under the shoulder (6 mm in front of the pin, 6 s into the processing), the material is subjected to flow at 576 K. And there is a significant weakening of the ND component compared to the LZ case. Closer to the pin (at about 633 K), the maximum has already shifted to about 20° off ND. At about 6 mm behind the pin in the stir zone (i.e., 21 s into the processing), the temperature reached the peak (640 K) and the initial ND component was completely dissipated to exhibit a strong single component texture at about 34°. This is qualitatively quite different from the shear texture observed in LZ case. At the wake of the tool and during cooling, the characteristics of the texture remains the same but the maximum intensifies markedly (from 11 to 23) and shifts slightly towards 30° off ND. This later development may be caused by a continuous dynamic recrystallization (CDRX) [71, 72] during the cooling cycle of the processing. For CDRX, the low angle grain boundaries are formed and develop into high angle grain boundaries, which is prevalent during the severe plastic deformation of Mg alloys [71, 72 , 73]. As the distance is away from the pin, the 30° off-ND texture component is intensified with the increasing of processing time. It is probably due to the grain boundaries convergency in the grain growth [64]. The HZ processing is overall a lower temperature process where the texture development is much more abrupt and starts occurring as low as 570 K and completes at around 630 ~ 640 K. At this temperature range, even under much slower strain rates than the estimated 9 s^{-1}, there could be significant twinning activities. For example, Li et al. [49] investigated the effect of thermo-mechanical input on the recrystallized grain size and development of texture of AZ31 Mg alloy during hot compression under a wide range of temperature, strain rate, and strain. The results showed that the texture exhibited a shear type with a diffuse distribution of (0002) poles along the ND-TD plane under relatively low Z conditions. On the other hand, under the Z of about 10^{14} and 10^{15} s^{-1} (similar to the current HZ condition), the deformation twinning activities became prevalent, which changed the recrystallization kinetics. There was an incubation period followed by a rapid recrystallization leading to a significant grain refinement. This twin-assisted recrystallization also produced a strong off-ND texture. Moreover, Yu et al. also reported the similar effects of the twin-assisted dynamic recrystallization on the grain refinement and texture development during a hot compression [59] and also FSP [5] of AZ31 Mg alloy. They also showed that both the through-thickness and in-plane hot compressions resulted in almost identical recrystallization microstructures and suggested that the involvement of the deformation twinning in the dynamic recrystallization and grain refinement are path independent and may prevail for the more complicated loading/flow patterns. Despite the more complex material flow expected during the FSP compared to the uniaxial studied conducted earlier [16, 40, 59], the texture developments during the FSP indicate that the process can be considered to be strongly governed by the Z parameter.

5. Conclusions

The time-of-flight neutron diffraction technique was used for an in-operando study on the real-time development of texture during the friction stir processing (FSP) of AZ31 Mg alloy. First, a series of in-situ, quasi-steady state measurements of the lattice parameters and integrated peak intensities were conducted as a function of the distance between the FSP tool pin and the diffraction measurement positions. Subsequently, the quasi-steady state measurement results were converted to a Lagrangian dataset representing a series of time-resolved snapshots of the transient material behavior during the FSP. As a result, the time-temperature-texture diagram was constructed that illustrate the development of texture and the evolution temperature during FSP as a function of the real processing time. Moreover, the study was conducted for two different thermo-mechanical processing conditions in terms of the Zener-Hollomon parameter (Z) to investigate the effect of Z on the resulting temperature profile and texture development during the FSP. The specific conclusions are as follows.

- The two FSP conditions studied are: (i) a low-Z processing using 1200 rpm tool rotation and 0.1 mm/s travel speed, corresponding to the Z of 4.5×10^{12} s^{-1} and (ii) a high-Z processing with 300 rpm,1 mm/s, and the Z of 3.1×10^{14} s^{-1}.
- Using the thermal lattice strains measured by neutron diffraction and the coefficient of thermal expansion, the temperature profile during FSP was estimated. For the LZ and HZ cases, the peak temperature reached at 775 K and 640 K, respectively.
- Using the integrated intensities of multiple reflections measured in situ along ND and RD during the FSP, (0002) pole figure (PF) was reconstructed. The current reconstruction method using the in-operando neutron data was validated by comparing the final texture to the post-mortem PF measured using a conventional texture measurement scheme. The results showed a good agreement for both LZ and HZ cases. The LZ FSP produced a shear texture often observed in the FSP Mg or Al alloy plates, whereas the HZ FSP generated a strong single-component off-ND texture.
- The time-temperature-texture diagrams for both LZ and HZ FSP were established using the reconstructed PFs and temperature profiles as a function of processing time.
- During the LZ FSP: After 60 s of processing (9 mm in front of the pin; 730 K), the strong basal texture started weakening and spread towards RD under the shoulder. After 90 s (6 mm in front of the pin; 772 K), the basal texture was further spread out towards RD. Immediately after the stirring (210 s; 6 mm behind the pin; peak temperature of 775 K), a broad spread of intensities along ND-RD plane was observed with the new maximum at 41° from ND. Typical FSP shear texture was fully formed with the RD components appearing as well after 240 s (9 mm behind the pin; 720 K). Further behind the pin at the wake (cooling to 670 K), the RD components continued to strengthen under the shoulder. Finally, during subsequent cooling to 630 K, the RD component weakened slightly and the maximum shifted to about 30º off ND.
- During the HZ FSP: After 6 s (9 mm in front of the pin; 576 K), the initial basal texture was significantly weakened. At 9 s (6 mm in front of the pin; 633 K), the maximum intensity shifted to 30º from ND. Immediately after the stirring (21 s; 6 mm behind the pin; peak temperature of 640 K), a strong single component texture was formed at 34º off ND, which is drastically different from the texture formed during the LZ processing. Subsequently, the characteristics of the texture remained the same but the maximum intensified significantly from the scale of 11 to 23 (multiples of a random distribution).
- The real-time, in-operando neutron diffraction measurements allowed the experimental observation of the texture development along with the changes in temperature during the FSP of a Mg alloy. The results show that the texture development can be strongly influenced by the key processing parameters and the Z value can be one of the texture design parameters even for the processing involving a complex materials flow. The neutron diffraction methodology used here can also be applied to other various transient materials behavior studies involving different manufacturing processes.

Acknowledgements

This research was supported by NSF Metals and Metallic Nanostructures (MMN) program under contract DMR-1308548. This research used resources at the Spallation Neutron Source, a DOE Office of Science User Facility operated by the Oak Ridge National Laboratory.

References

[1] R.S. Mishra, Z. Ma, Friction stir welding and processing, Materials Science and Engineering: R: Reports 50(1-2) (2005) 1-78.
[2] P. Threadgill, A. Leonard, H. Shercliff, P. Withers, Friction stir welding of aluminium alloys, International Materials Reviews 54(2) (2009) 49-93.
[3] Z.Y. Ma, R.S. Mishra, M.W. Mahoney, Superplastic deformation behaviour of friction stir processed 7075Al alloy, Acta Mater. 50(17) (2002) 4419-4430.
[4] C.J. Hsu, C.Y. Chang, P.W. Kao, N.J. Ho, C.P. Chang, Al-Al3Ti nanocomposites produced in situ by friction stir processing, Acta Mater. 54(19) (2006) 5241-5249.
[5] Z. Yu, H. Choo, Z. Feng, S.C. Vogel, Influence of thermo-mechanical parameters on texture and tensile behavior of friction stir processed Mg alloy, Scripta Mater 63(11) (2010) 1112-1115.
[6] G. Mann, J.R. Griffiths, C.H. Cáceres, Hall-Petch parameters in tension and compression in cast Mg–2Zn alloys, Journal of Alloys and Compounds 378(1-2) (2004) 188-191.
[7] D.L. Yin, J.T. Wang, J.Q. Liu, X. Zhao, On tension–compression yield asymmetry in an extruded Mg–3Al–1Zn alloy, Journal of Alloys and Compounds 478(1) (2009) 789-795.
[8] R. Armstrong, I. Codd, R. Douthwaite, N. Petch, The plastic deformation of polycrystalline aggregates, The Philosophical Magazine: A Journal of Theoretical Experimental and Applied Physics 7(73) (1962) 45-58.
[9] Y. Wang, H. Choo, Influence of texture on Hall–Petch relationships in an Mg alloy, Acta Mater. 81 (2014) 83-97.
[10] Y. Li, Dynamic Recrystallization of a Mg alloy during Friction Stir Processing: Grain Size Refinement and Texture Evolution, (2019).
[11] B.C. Wonsiewicz, Plasticity of magnesium crystals, Massachusetts Institute of Technology, 1966.
[12] H. Yu, Y. Xin, M. Wang, Q. Liu, Hall-Petch relationship in Mg alloys: A review, Journal of Materials Science & Technology 34(2) (2018) 248-256.
[13] A. Imandoust, C. Barrett, T. Al-Samman, K. Inal, H. El Kadiri, A review on the effect of rare-earth elements on texture evolution during processing of magnesium alloys, Journal of materials science 52 (2017) 1-29.
[14] S. Yi, J. Bohlen, F. Heinemann, D. Letzig, Mechanical anisotropy and deep drawing behaviour of AZ31 and ZE10 magnesium alloy sheets, Acta Mater. 58(2) (2010) 592-605.
[15] M. Bian, T. Sasaki, T. Nakata, Y. Yoshida, N. Kawabe, S. Kamado, K. Hono, Bake-hardenable Mg–Al–Zn–Mn–Ca sheet alloy processed by twin-roll casting, Acta Mater. 158 (2018) 278-288.
[16] Y. Li, P. Hou, Z. Wu, Z. Feng, Y. Ren, H. Choo, Dynamic recrystallization of a wrought magnesium alloy: Grain size and texture maps and their application for mechanical behavior predictions, Materials & Design 202 (2021) 109562.
[17] R. Xin, D. Liu, X. Shu, B. Li, X. Yang, Q. Liu, Influence of welding parameter on texture distribution and plastic deformation behavior of as-rolled AZ31 Mg alloys, Journal of Alloys and Compounds 670 (2016) 64-71.
[18] M.S. Kim, J.Y. Jung, Y.M. Song, S.H. Choi, Simulation of microtexture developments in the stir zone of friction stir-welded AZ31 Mg alloys, Int. J. Plast. 94 (2017) 24-43.
[19] M. Guerra, C. Schmidt, J.C. McClure, L. Murr, A. Nunes, Flow patterns during friction stir welding, Materials characterization 49(2) (2002) 95-101.
[20] K. Kumar, S.V. Kailas, The role of friction stir welding tool on material flow and weld formation, Materials Science and Engineering: A 485(1-2) (2008) 367-374.
[21] C. Chang, X. Du, J. Huang, Achieving ultrafine grain size in Mg–Al–Zn alloy by friction stir processing, Scripta Materialia 57(3) (2007) 209-212.
[22] C. Chang, C. Lee, J. Huang, Relationship between grain size and Zener–Holloman parameter during friction stir processing in AZ31 Mg alloys, Scripta materialia 51(6) (2004) 509-514.
[23] X. Feng, H. Liu, S.S. Babu, Effect of grain size refinement and precipitation reactions on strengthening in friction stir processed Al–Cu alloys, Scripta Materialia 65(12) (2011) 1057-1060.

[24] W. Woo, H. Choo, D.W. Brown, S.C. Vogel, P.K. Liaw, Z. Feng, Texture analysis of a friction stir processed 6061-T6 aluminum alloy using neutron diffraction, Acta Mater. 54(15) (2006) 3871-3882.
[25] W. Woo, H. Choo, D. Brown, Z. Feng, P. Liaw, S. David, C. Hubbard, M. Bourke, Effect of Heat and Plastic Deformation on the Texture of a Friction Stir Processed 6061-T6 Aluminum Alloy: A Neutron Diffraction Study, Trends In Welding Research: Proceedings of the 7Th International Conference, ASM International, 2006, p. 393.
[26] W. Woo, H. Choo, M.B. Prime, Z. Feng, B. Clausen, Microstructure, texture and residual stress in a friction-stir-processed AZ31B magnesium alloy, Acta Mater. 56(8) (2008) 1701-1711.
[27] W. Woo, H. Choo, D.W. Brown, M.A.M. Bourke, Z. Feng, S.A. David, C.R. Hubbard, P.K. Liaw, Deconvoluting the influences of heat and plastic deformation on internal strains generated by friction stir processing, Applied Physics Letters 86(23) (2005) 231902.
[28] W. Woo, H. Choo, P.J. Withers, Z. Feng, Prediction of hardness minimum locations during natural aging in an aluminum alloy 6061-T6 friction stir weld, Journal of Materials Science 44(23) (2009) 6302-6309.
[29] W. Woo, H. Choo, Softening behaviour of friction stir welded Al 6061-T6 and Mg AZ31B alloys, Sci. Technol. Weld. Join. 16(3) (2011) 267-272.
[30] Z. Yu, Z. Feng, H. Choo, S. Vogel, Texture Modification and Ductility Enhancement in Mg Alloy Through Friction Stir Processing, ASME International Mechanical Engineering Congress and Exposition, 2011, pp. 523-527.
[31] W. Woo, H. Choo, D.W. Brown, P.K. Liaw, Z. Feng, Texture variation and its influence on the tensile behavior of a friction-stir processed magnesium alloy, Scripta Materialia 54(11) (2006) 1859-1864.
[32] Y.N. Wang, C.I. Chang, C.J. Lee, H.K. Lin, J.C. Huang, Texture and weak grain size dependence in friction stir processed Mg-Al-Zn alloy, Scripta Mater 55(7) (2006) 637-640.
[33] R.L. Xin, B. Li, A.L. Liao, Z. Zhou, Q. Liu, Correlation Between Texture Variation and Transverse Tensile Behavior of Friction-Stir-Processed AZ31 Mg Alloy, Metallurgical and Materials Transactions a-Physical Metallurgy and Materials Science 43A(7) (2012) 2500-2508.
[34] P. Cavaliere, P.P. De Marco, Friction stir processing of AM60B magnesium alloy sheets, Materials Science and Engineering A 462(1-2) (2007) 393-397.
[35] L.L. Huetsch, J.F. dos Santos, N. Huber, Investigations of microstructural, thermal and local strain phenomena of high speed friction stir processed Mg AZ31, Proceedings of the 1st International Joint Symposium on Joining and Welding (2013) 59-65.
[36] W. Yuan, R. Mishra, B. Carlson, R. Verma, R. Mishra, Material flow and microstructural evolution during friction stir spot welding of AZ31 magnesium alloy, Materials science and engineering: A 543 (2012) 200-209.
[37] S. Mironov, T. Onuma, Y.S. Sato, H. Kokawa, Microstructure evolution during friction-stir welding of AZ31 magnesium alloy, Acta Mater. 100 (2015) 301-312.
[38] R. Nandan, G.G. Roy, T.J. Lienert, T. Debroy, Three-dimensional heat and material flow during friction stir welding of mild steel, Acta Mater. 55(3) (2007) 883-895.
[39] A.P. Reynolds, Flow visualization and simulation in FSW, Scripta Materialia 58(5) (2008) 338-342.
[40] Z. Yu, W. Zhang, H. Choo, Z. Feng, Transient Heat and Material Flow Modeling of Friction Stir Processing of Magnesium Alloy using Threaded Tool, Metallurgical and Materials Transactions A 43(2) (2012) 724-737.
[41] M.L. Wissink, Y. Chen, M.J. Frost, S.J. Curran, O. Rios, Z.C. Sims, D. Weiss, E.T. Stromme, K. An, Operando measurement of lattice strain in internal combustion engine components by neutron diffraction, Proceedings of the National Academy of Sciences 117(52) (2020) 33061-33071.
[42] W. Woo, Z. Feng, X.L. Wang, D.W. Brown, B. Clausen, K. An, H. Choo, C.R. Hubbard, S.A. David, In situ neutron diffraction measurements of temperature and stresses during friction stir welding of 6061-T6 aluminium alloy, Sci. Technol. Weld. Join. 12(4) (2007) 298-303.
[43] W. Woo, Z. Feng, B. Clausen, S.A. David, In situ neutron diffraction analyses of temperature and stresses during friction stir processing of Mg-3Al-1Zn magnesium alloy, Mater. Lett. 196 (2017) 284-287.

[44] M.R. Barnett, A taylor model based description of the proof stress of magnesium AZ31 during hot working, Metallurgical and Materials Transactions A 34(9) 1799-1806.
[45] M.R. Barnett, Z. Keshavarz, A.G. Beer, D. Atwell, Influence of grain size on the compressive deformation of wrought Mg–3Al–1Zn, Acta Mater. 52(17) (2004) 5093-5103.
[46] C.M. Cepeda-Jiménez, J.M. Molina-Aldareguia, M.T. Pérez-Prado, Origin of the twinning to slip transition with grain size refinement, with decreasing strain rate and with increasing temperature in magnesium, Acta Mater. 88 (2015) 232-244.
[47] Z. Yu, H. Choo, Influence of twinning on the grain refinement during high-temperature deformation in a magnesium alloy, Scripta Materialia 64(5) (2011) 434-437.
[48] M.R. Barnett, D. Atwell, A.G. Beer, Effect of grain size on the deformation and dynamic recrystallization of Mg-3Al-1Zn, Materials Science Forum, Trans Tech Publ, 2004, pp. 435-440.
[49] Y. Li, P. Hou, Z. Wu, Z. Feng, Y. Ren, H. Choo, Dynamic recrystallization of a wrought magnesium alloy: Grain size and texture maps and their application for mechanical behavior predictions, Materials & Design 202 (2021).
[50] F. Bachmann, R. Hielscher, H. Schaeben, Texture analysis with MTEX–free and open source software toolbox, Solid State Phenomena, Trans Tech Publ, 2010, pp. 63-68.
[51] B.H. Toby, R.B. Von Dreele, GSAS-II: the genesis of a modern open-source all purpose crystallography software package, Journal of Applied Crystallography 46(2) (2013) 544-549.
[52] M. Daymond, M. Bourke, R. Von Dreele, Use of Rietveld refinement to fit a hexagonal crystal structure in the presence of elastic and plastic anisotropy, Journal of applied physics 85(2) (1999) 739-747.
[53] Y. Touloukian, R. Powell, C. Ho, M. Nicolaou, Thermophysical properties of matter-The TPRC data series. Volume 10. Thermal Diffusivity, Thermophysical and Electronic Properties Information Analysis Center, 1974.
[54] P. Lukáč, Z. Trojanová, J. Džugan, K. Halmešová, Mechanical and physical properties of Mg alloys prepared by SPD methods, IOP Conference Series: Materials Science and Engineering, IOP Publishing, 2021, p. 012042.
[55] H. Yang, L. Huang, M. Zhan, Hot forming characteristics of magnesium alloy AZ31 and three-dimensional FE modelling and simulation of the hot splitting spinning process, Magnesium Alloys-Design, Processing and Properties (2011) 367-388.
[56] A. Nunes, Heat input and temperature distribution in friction stir welding, J Mater Process Manuf Sci 7 (1998) 163.
[57] Y.J. Chao, X. Qi, W. Tang, Heat transfer in friction stir welding—experimental and numerical studies, J. Manuf. Sci. Eng. 125(1) (2003) 138-145.
[58] Z. Yu, W. Zhang, H. Choo, Z. Feng, Transient heat and material flow modeling of friction stir processing of magnesium alloy using threaded tool, Metallurgical and Materials Transactions A 43 (2012) 724-737.
[59] Z. Yu, H. Choo, Influence of twinning on the grain refinement during high-temperature deformation in a magnesium alloy, Scripta Materialia 5(64) (2011) 434-437.
[60] C. Windsor, Pulsed neutron scattering, Taylor and Francis, London, 1981.
[61] S.H.C. Park, Y.S. Sato, H. Kokawa, Basal plane texture and flow pattern in friction stir weld of a magnesium alloy, Metallurgical and Materials Transactions A 34 (2003) 987-994.
[62] D.P. Field, T.W. Nelson, Y. Hovanski, K.V. Jata, Heterogeneity of crystallographic texture in friction stir welds of aluminum, Metallurgical and Materials Transactions A 32 (2001) 2869-2877.
[63] Y.S. Sato, H. Kokawa, K. Ikeda, M. Enomoto, T. Hashimoto, S. Jogan, Microtexture in the friction-stir weld of an aluminum alloy, Metallurgical and Materials Transactions A 32 (2001) 941-948.
[64] U. Suhuddin, S. Mironov, Y. Sato, H. Kokawa, Grain structure and texture evolution during friction stir welding of thin 6016 aluminum alloy sheets, Materials Science and Engineering: A 527(7-8) (2010) 1962-1969.

[65] S.R. Agnew, P. Mehrotra, T.M. Lillo, G.M. Stoica, P.K. Liaw, Texture evolution of five wrought magnesium alloys during route A equal channel angular extrusion: Experiments and simulations, Acta Mater. 53(11) (2005) 3135-3146.

[66] W.J. Kim, S.I. Hong, Y.S. Kim, S.H. Min, H.T. Jeong, J.D. Lee, Texture development and its effect on mechanical properties of an AZ61 Mg alloy fabricated by equal channel angular pressing, Acta Mater. 51(11) (2003) 3293-3307.

[67] W. Woo, Z. Feng, X.-L. Wang, K. An, C.R. Hubbard, S.A. David, H. Choo, In situ neutron diffraction measurement of transient temperature and stress fields in a thin plate, Applied physics letters 88(26) (2006) 261903.

[68] Y. Xin, H. Zhou, H. Yu, R. Hong, H. Zhang, Q. Liu, Controlling the recrystallization behavior of a Mg–3Al–1Zn alloy containing extension twins, Materials Science and Engineering: A 622 (2015) 178-183.

[69] Y. Xin, H. Zhou, G. Wu, H. Yu, A. Chapuis, Q. Liu, A twin size effect on thermally activated twin boundary migration in a Mg–3Al–1Zn alloy, Materials Science and Engineering: A 639 (2015) 534-539.

[70] D. Song, T. Zhou, J. Tu, L. Shi, B. Song, L. Hu, M. Yang, Q. Chen, L. Lu, Improved stretch formability of AZ31 sheet via texture control by introducing a continuous bending channel into equal channel angular rolling, Journal of Materials Processing Technology 259 (2018) 380-386.

[71] C.I. Chang, X.H. Du, J.C. Huang, Producing nanograined microstructure in Mg–Al–Zn alloy by two-step friction stir processing, Scripta Materialia 59(3) (2008) 356-359.

[72] A.H. Feng, Z.Y. Ma, Microstructural evolution of cast Mg–Al–Zn during friction stir processing and subsequent aging, Acta Mater. 57(14) (2009) 4248-4260.

[73] H. Jia, Y. Li, Texture evolution of an Al-8Zn alloy during ECAP and post-ECAP isothermal annealing, Materials Characterization 155 (2019) 109794.

Table 1. Friction stir processing conditions and the calculation of Zener-Hollomon parameter (Z) based on the processing parameters and the activation energy of 164 kJ/mol [47, 49]. The peak temperature, average strain rate, and the Z values for the stir zone are empirically calculated following [5, 22, 44-49].

Rotation speed (rpm)	Travel speed (mm/s)	Peak temperature (K)	Strain rate (s^{-1})	Z (s^{-1})
1200	0.1	783	37	3.3E12
300	1	608	9	1.2E15

Table 2. The angles and normalized intensity ratios between (0002) and $(10\bar{1}l)$ reflections are calculated for the reconstruction of the distribution and magnitude of (0002) intensities on the (0002) PF. The *a* and *c* lattice parameters of 3.19 Å and 5.19 Å are used for the calculations of the angles for the Mg alloy.

Plane	Angle to (0002)	Calculated intensity ratio, R
(0002)	0°	1
$(10\bar{1}5)$	21°	0.09
$(10\bar{1}3)$	32°	0.46
$(10\bar{1}2)$	43°	0.43
$(10\bar{1}1)$	62°	3.53

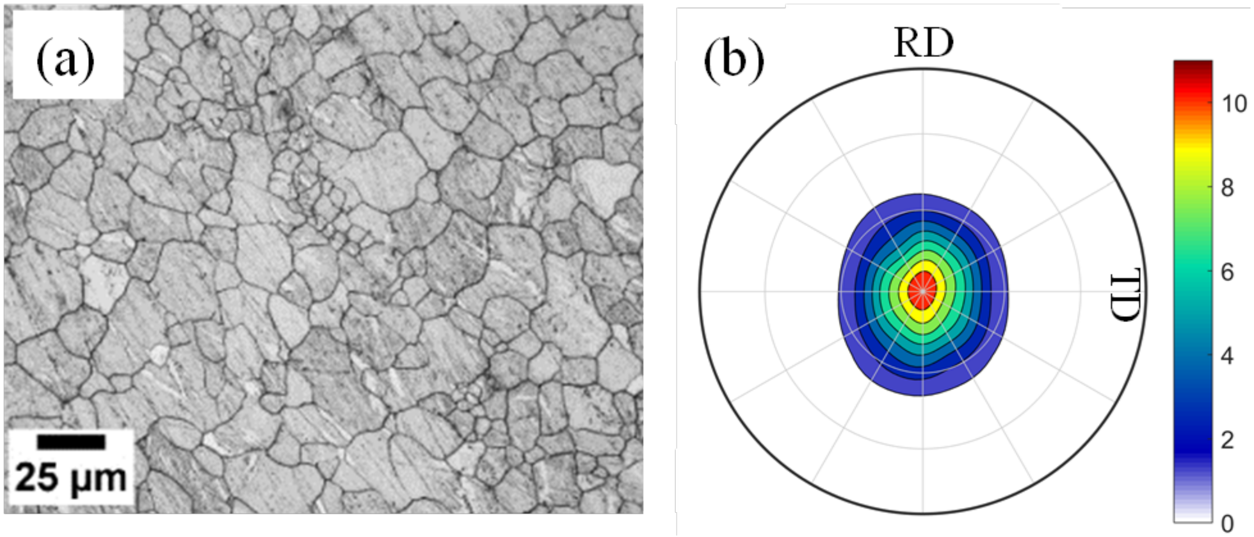

Figure 1. As-received AZ31B Mg alloy plate: (a) microstructure and (b) (0002) pole figure.

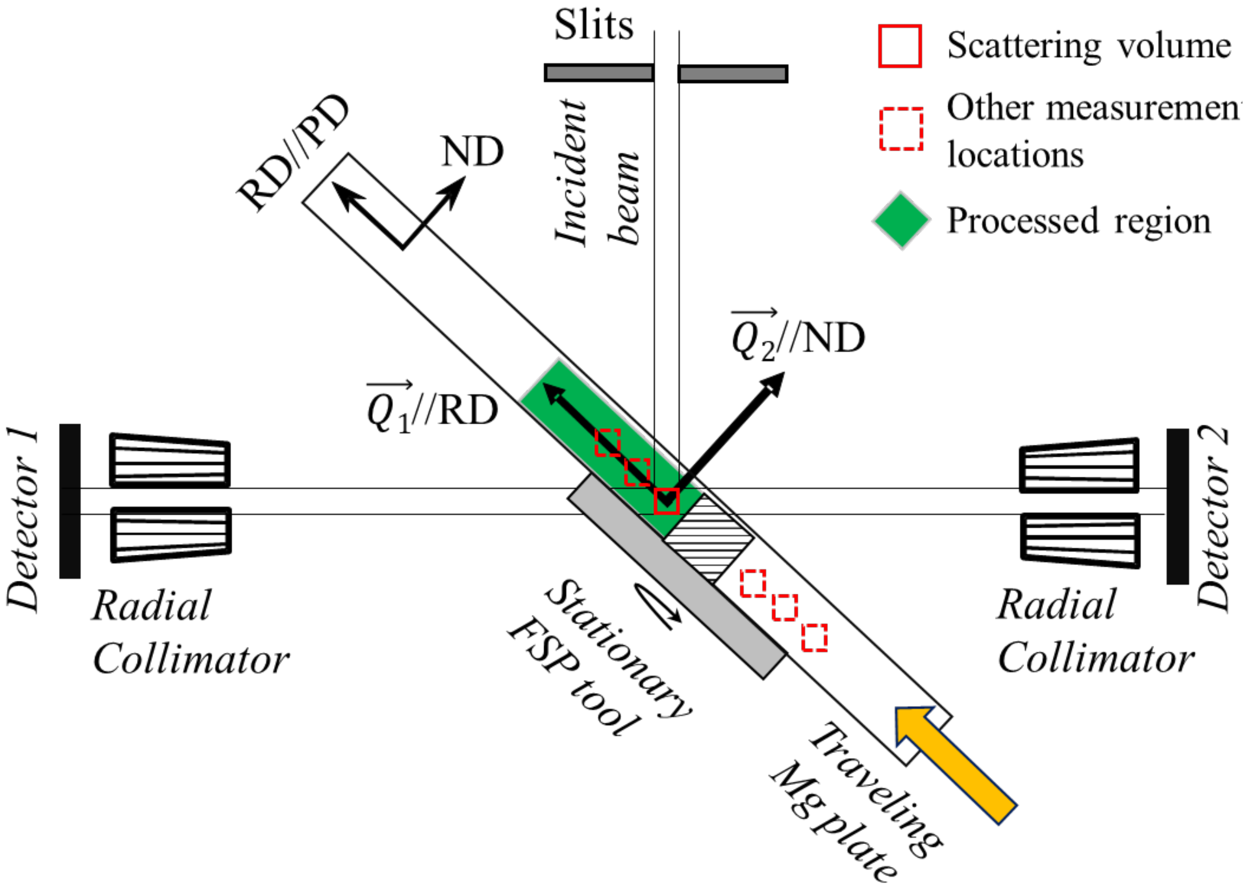

Figure 2. Schematic of the in-situ neutron diffraction measurement setup at the VULCAN beamline. Top view shows that the potable FSP machine is laid sideways and the FSP tool rotates at a fixed position, while the Mg alloy plate travels as indicated with a yellow arrow. The processed region behind the rotating FSP tool is marked with a green box. Note that RD, PD, and ND refer to the rolling, processing, and normal directions of the plate, respectively. Also shown are the incident neutron beam, the scattering volume (i.e., the current measurement location marked with a solid red box), and diffracted neutron beams reaching the two detector systems. Note that the in-situ neutron diffraction measurements were conducted as a function of the distance between the scattering volume and the tool pin, for each distance case using a new Mg plate. A series of other measurement locations are also marked with red boxes (dotted line).

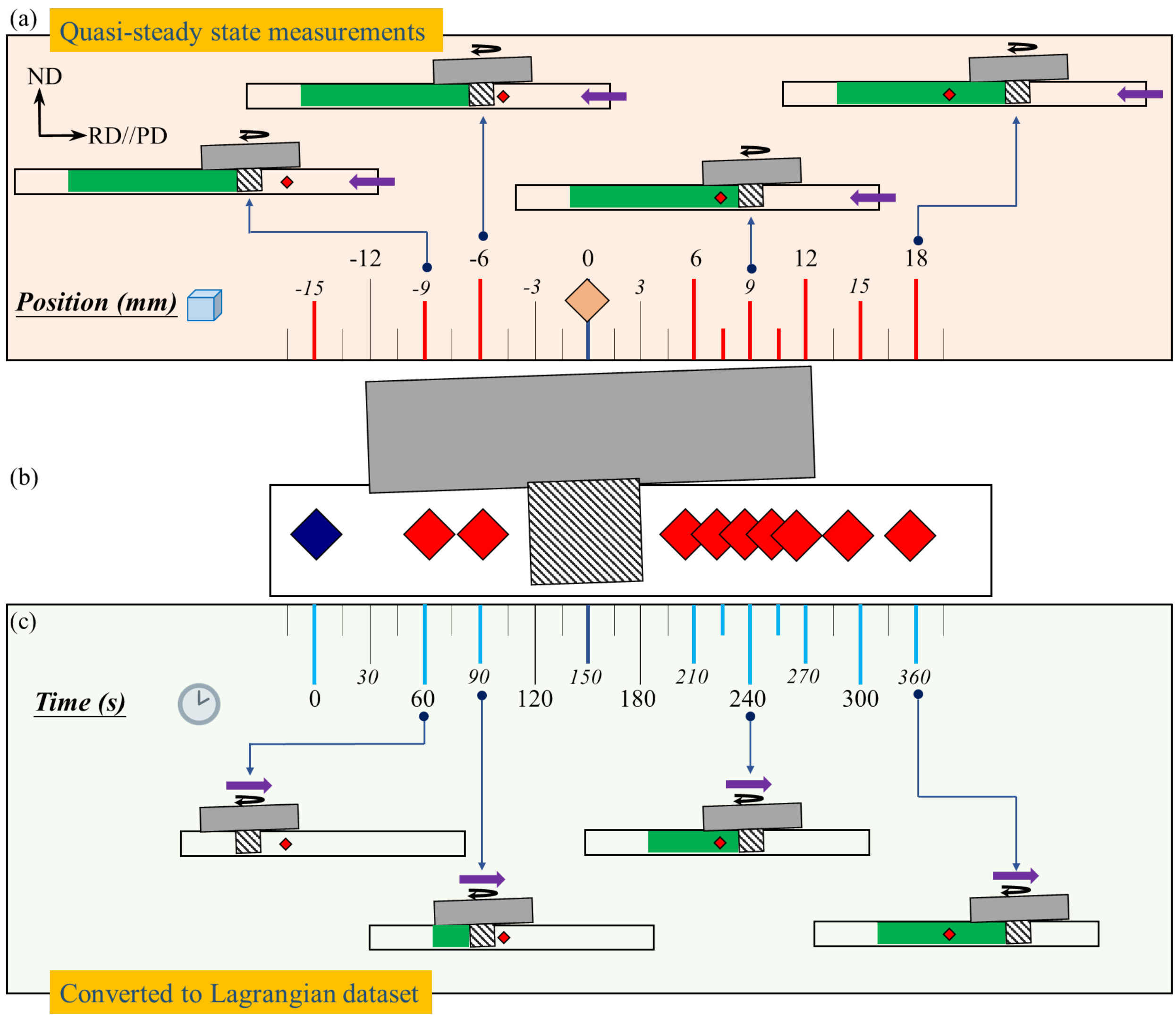

Figure 3. In-situ neutron diffraction measurements and a conversion from Eulerian to Lagrangian dataset to probe time-resolved transient behavior during FSP. The example shown here is for the LZ case. (a) Various quasi-steady state measurement positions in the Mg plate at different distances (mm) from the tool pin. (b) A schematic showing all measurement positions in the plate. (c) The conversion of a dataset measured as a function of the distance (mm) in (a) to a dataset "measured" as a function of time (s) during processing.

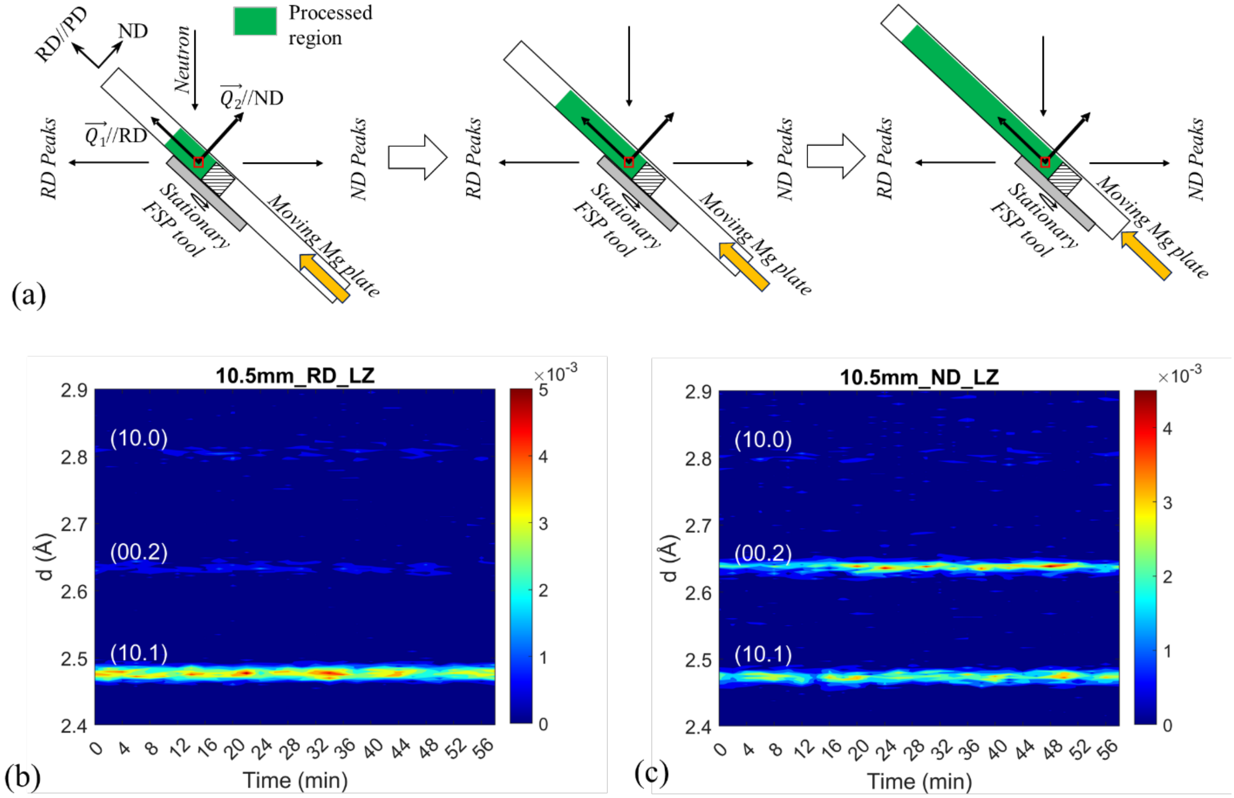

Figure 4. In-situ neutron diffraction data measured during FSP. Example here shows a quasi-steady state measurement conducted at +10.5 mm position (red box) at the wake of the FSP in the processed region (green region) for about 60 minutes during an LZ FSP. The stationary FSP tool was rotating at 1200 rpm and the Mg plate traveled at 0.1 mm/s. (a) Schematics showing three different timeframes during the measurement. Contour plots of a series of time-of-flight diffraction patterns (d vs. intensity) presented as a function of time during the FSP are presented for: (b) detector bank 1 (i.e., RD patterns) and (c) detector bank 2 (i.e., ND patterns). The analysis of these diffraction patterns showed that the lattice parameters and integrated peak intensities reached a steady state during which a time-averaged lattice parameter and intensity values are obtained. These results are presented in Figures 5 and 6.

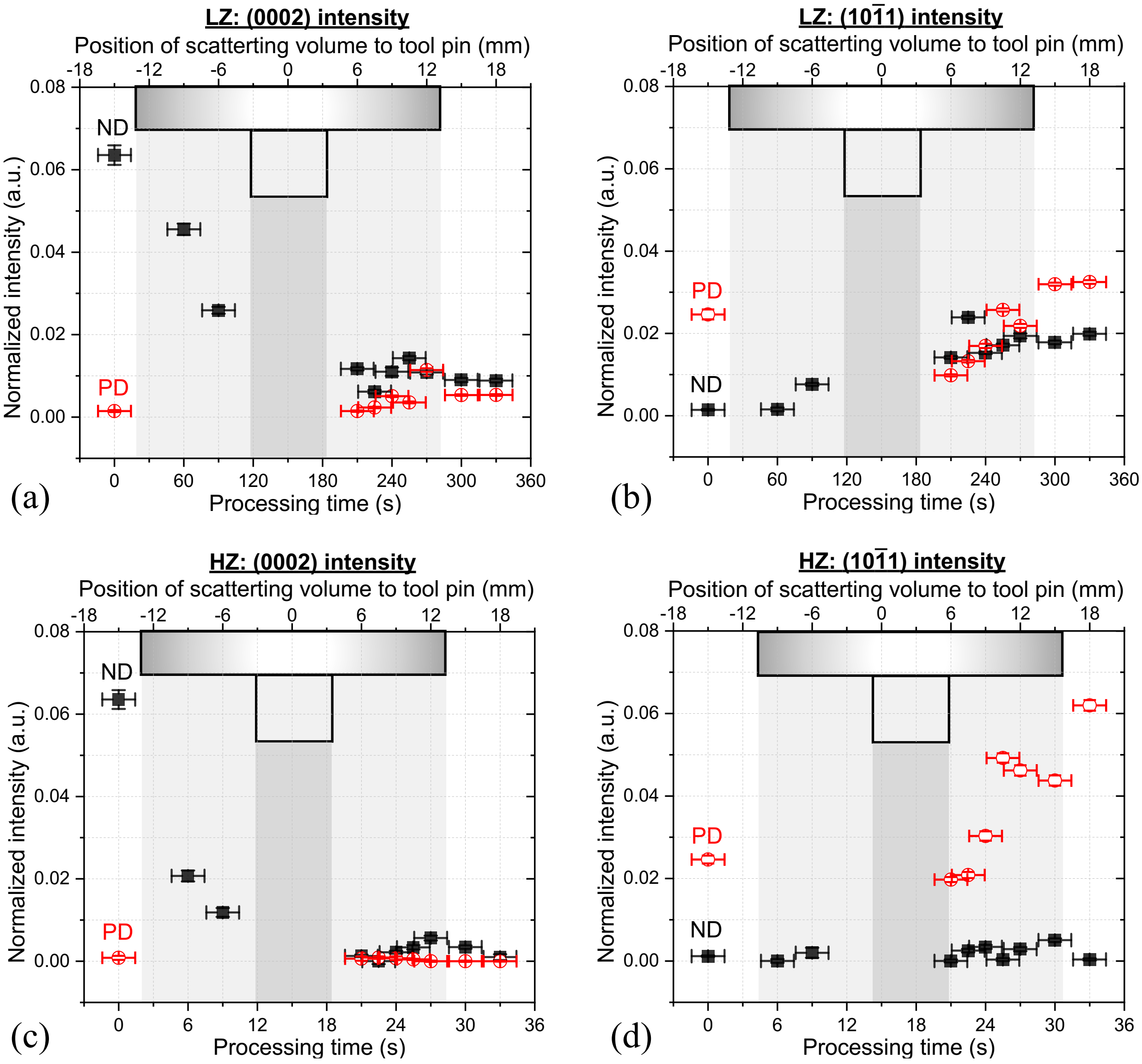

Figure 5. Evolution of integrated peak intensities measured along ND and PD (//RD) during the FSP presented as a function of both the distance between the tool pin and the scattering volume (top x-axis) and also the processing time (bottom x-axis). (a) LZ (0002), (b) LZ $(10\bar{1}1)$, (c) HZ (0002), and (d) HZ $(10\bar{1}1)$. Note that the FSP tool shoulder and pin are shown on the top x-axis.

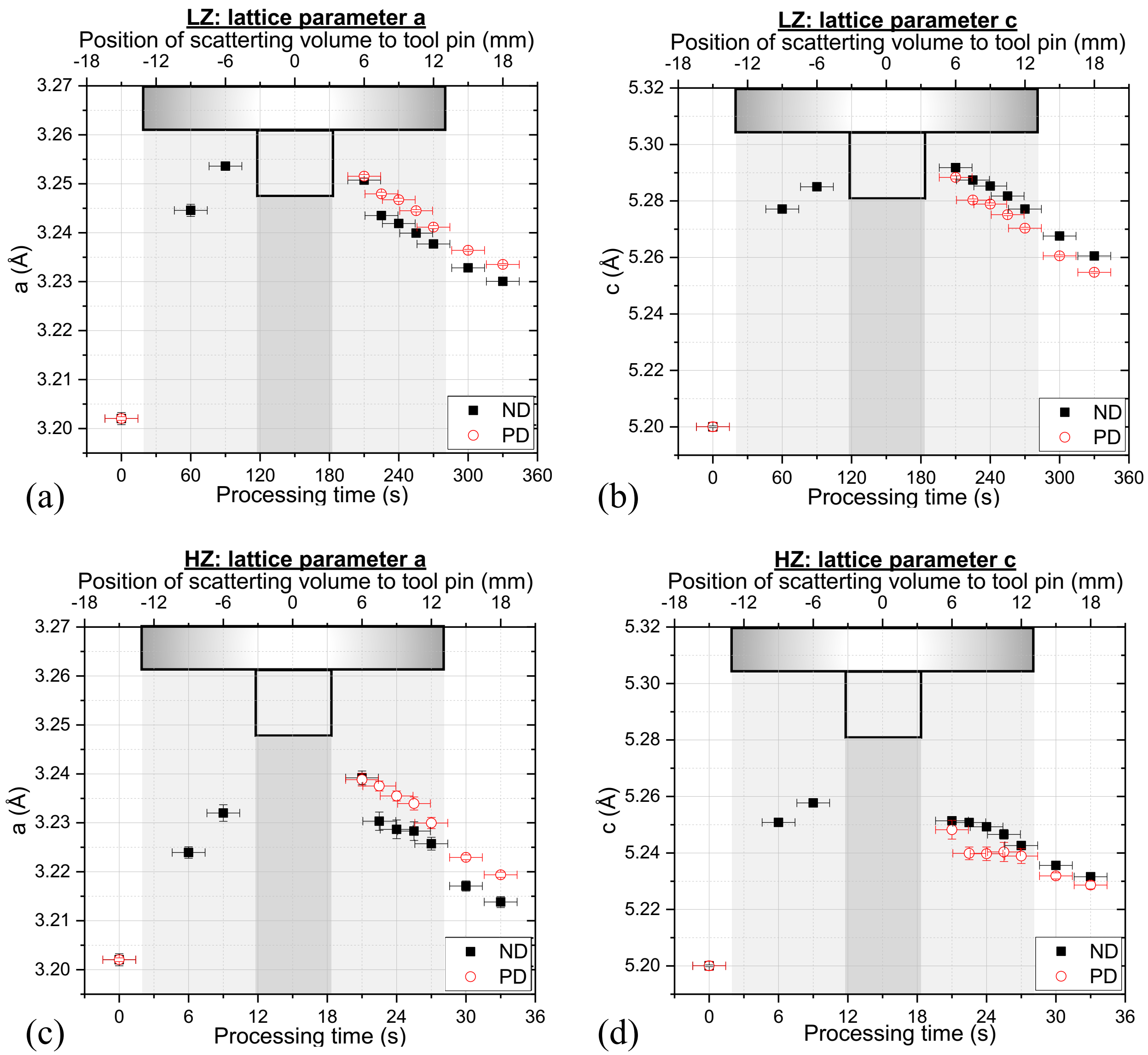

Figure 6. Evolution of lattice parameters measured along ND and PD (//RD) during the FSP presented as a function of both the distance between the tool pin and the scattering volume (top x-axis) and also the processing time (bottom x-axis). (a) LZ a-axis, (b) LZ c-axis, (c) HZ a-axis, and (d) HZ c-axis. Note that the FSP tool shoulder and pin are shown on the top x-axis.

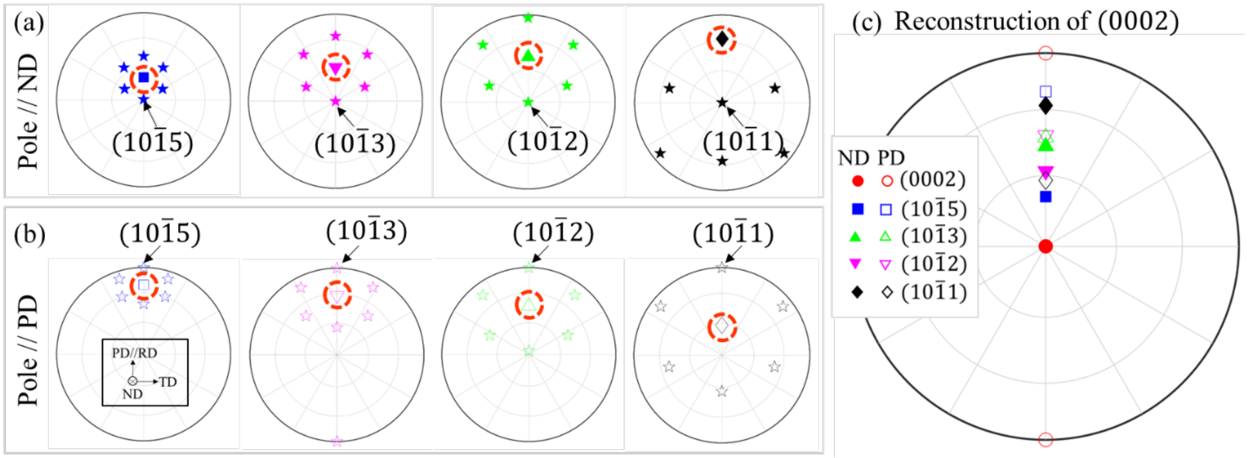

Figure 7. Reconstruction of the distribution of (0002) poles on the (0002) PF using measured intensities of (0002), $(10\bar{1}5)$, $(10\bar{1}3)$, $(10\bar{1}2)$ and $(10\bar{1}1)$ from the ND and RD(//PD) neutron detectors. (a) Angular positions of (0002) poles on the PF according to the $(10\bar{1}l)$ poles measured along ND during the neutron diffraction. The black arrow points to the measured data point. The four red circles indicate the (0002) variants selected from each $(10\bar{1}l)$ on the ND-RD plane towards the RD(//PD) orientation. (b) Angular positions of (0002) poles on the PF according to the $(10\bar{1}l)$ poles measured along RD(//PD) during the neutron diffraction. (c) Compilation of (a) and (b) showing the distribution of (0002) poles that can be rendered on the PF according to all $(10\bar{1}l)$ reflections as well as the (0002) itself measured along ND and RD.

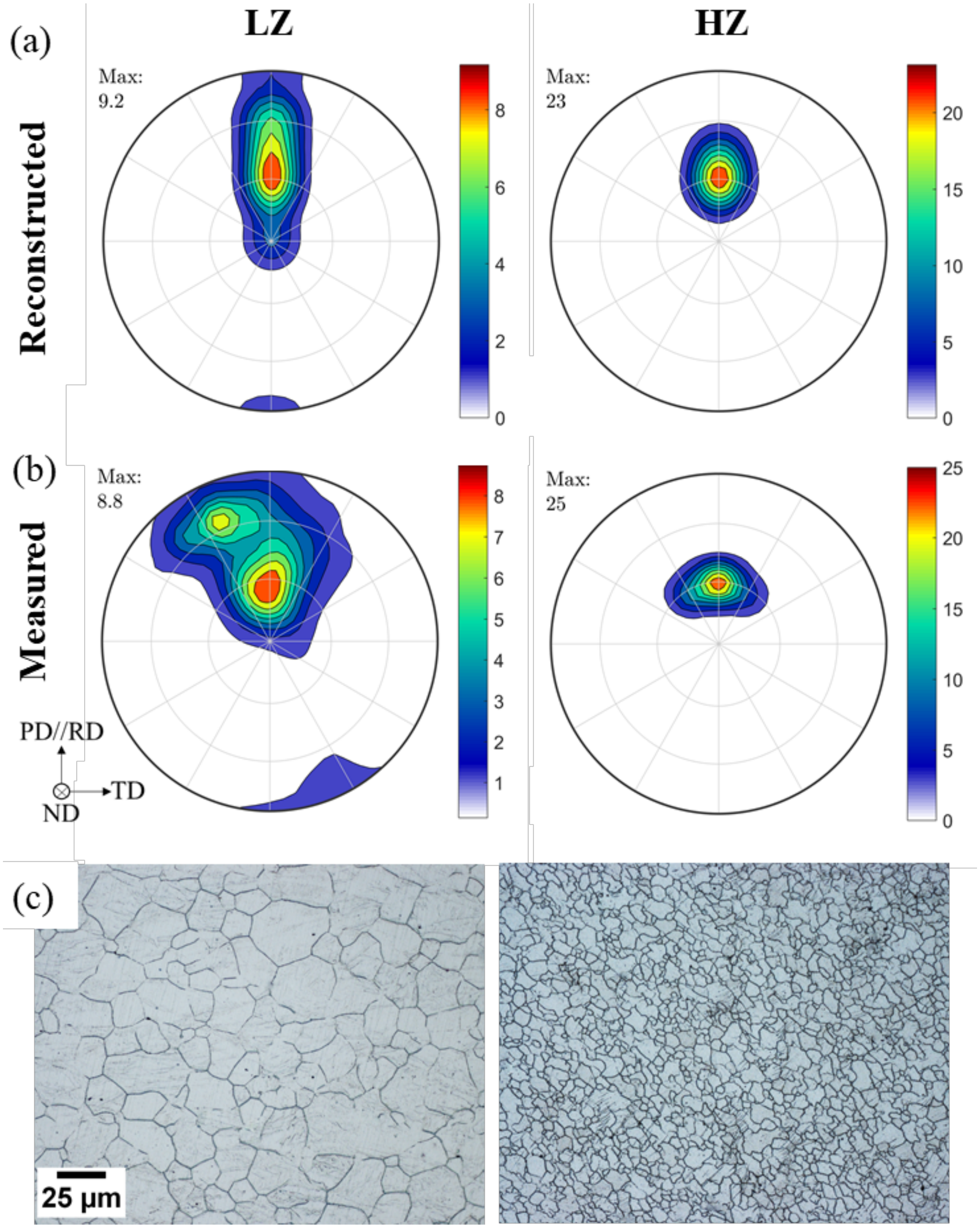

Figure 8. Comparison between the reconstructed and measured (0002) PFs in the stir zone after the FSP under LZ and HZ conditions. Also presented are the corresponding light optical micrographs. (a) Reconstructed PFs based on the in-situ neutron diffraction data measured during the FSP. (b) Measured PFs with a full pole coverage using post-mortem samples extracted from the FSP plates. (c) Optical micrographs of the stir zone processed under the LZ and HZ conditions.

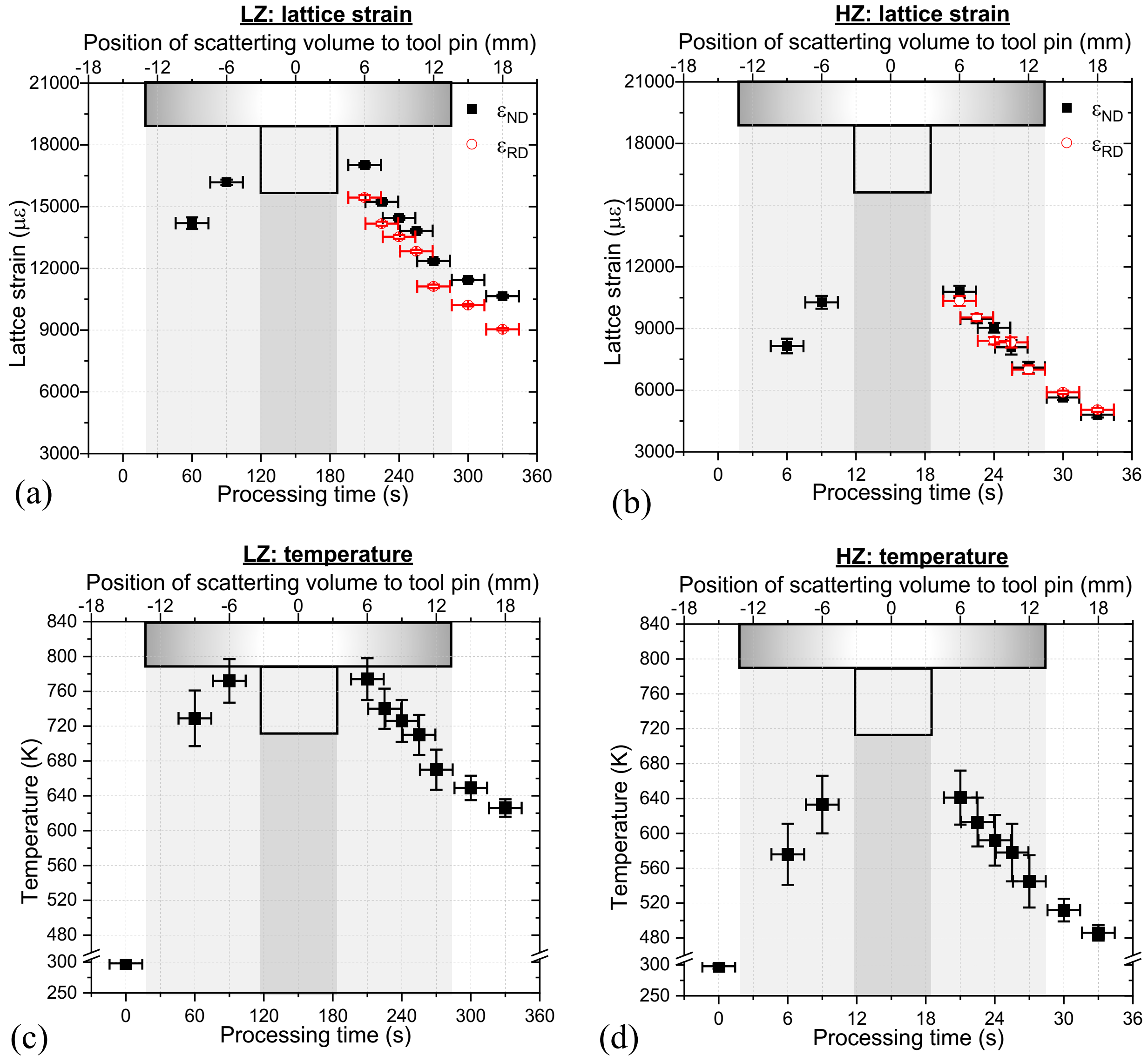

Figure 9. The apparent lattice strains (ε_{RD} and ε_{ND}) and temperature profiles are presented as a function of both the distance between the tool pin and the scattering volume (top x-axis) and also the processing time (bottom x-axis) for LZ and HZ conditions. Note that the FSP tool shoulder and pin are shown on the top x-axis. (a) LZ apparent lattice strain, (b) HZ apparent lattice strain, (c) LZ temperature, and (d) HZ temperature.

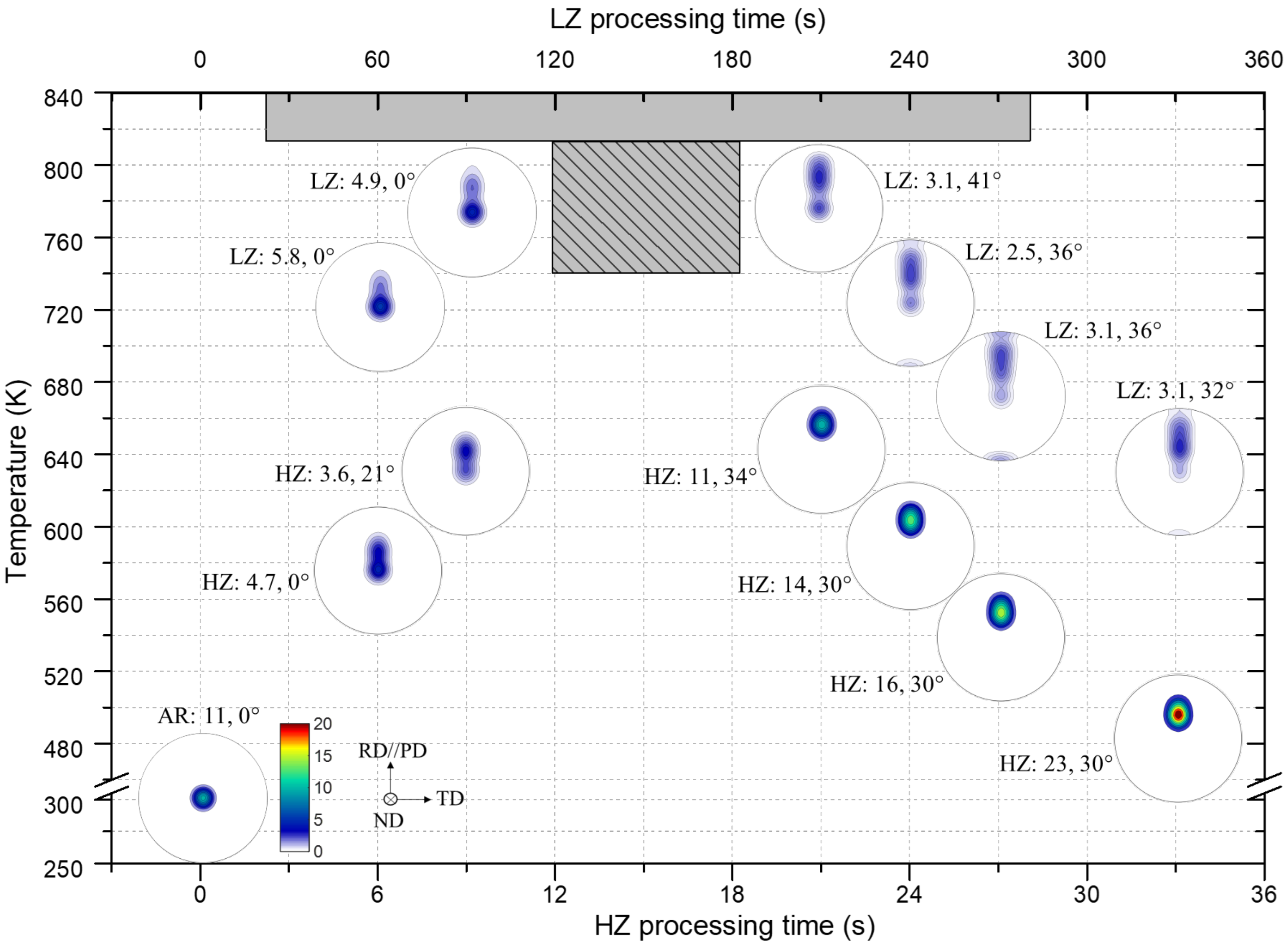

Figure 10. Time-temperature-texture diagram for the FSP Mg alloy. The real-time evolutions of (0002) PFs and the temperature are presented as a function of the processing time for both LZ and HZ cases. The center of each PF marks the corresponding time and temperature. Also, for each PF, the maximum pole intensity and its location are noted. For example, (HZ: 3.6, 21°) indicates maximum intensity of 3.6 at 21° from the ND pole towards the RD pole on the ND-RD plane.